Chapter 5

Fracture toughness characterization of ductile phase containing in-situ BMG composite

Fracture toughness of ductile phase containing in-situ BMG composites is studied. Unlike monolithic BMG's, the composites show stable crack growth and crack arrest. Increasing the volume fraction of ductile dendrite phase with fully developed microstructure, produced by semi-solid processing, increases the amount of energy needed to advance pre-existing cracks. Although a standard evaluation of fracture toughness is not available at this point, due to sample geometry limitations, J-R curve evaluation of the composite reveals significant improvements in fracture toughness, having values that may exceed 136 $MPa \cdot m^{1/2}$.

5.1 Introduction

Although the bulk metallic glasses (BMG's) are known to have high fracture toughness, fracture behavior of monolithic BMG's is unstable. As described in Figure 5-1, a monolithic BMG fracture specimen shows linear behavior almost up to the critical load and, at the moment of crack-initiation, propagation occurs through the entire specimen, fracturing it. However, by introducing a ductile phase, formed homogeneously during cooling inside the BMG matrix [1,2], stable crack growth is achieved [3]. This is a result of the confinement effect of shear band propagation. The recent discovery of a high-toughness monolithic BMG with extremely large supercooled liquid region [4] and subsequent application of this BMG as the matrix for an in-situ composite with controlled microstructural characteristic length scale [5, 6] maximized the toughening effect. In order to characterize this highly-toughened BMG composite material, elastic-plastic fracture mechanics were used to describe the extensive plasticity before the initial crack propagation. In this chapter, fracture tests on the new composite were performed and the elastic-plastic fracture parameter (J) was evaluated.

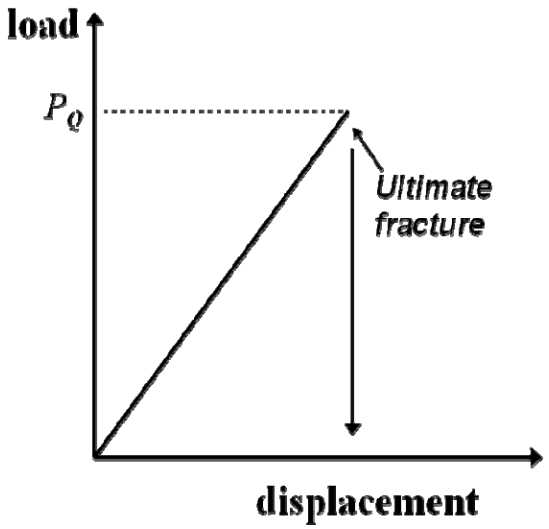

Figure 5-1. Typical fracture behavior of monolithic BMG.

5.2 Ductile phase containing in-situ BMG composite

Recently, significant improvements in the mechanical properties of ductile phase containing in-situ BMG composite have been achieved by Hofmann et al. [5, 6]. Compared to the previous in-situ composites developed by Kim et al. [1, 2], the new BMG composites have the following features:

(1) Increased Ti content and removal of Ni to reduce density. Removal of Ni is also known to enhance fracture toughness of the glass and suppress possible nucleation of brittle intermetallic crystalline phases during processing [4, 7, 8].

(2) A homogeneous and coarsened microstructure. Earlier composites had cooling rate dependent microstructures. Ingots cooled from above the alloy liquidus showed large variations in the overall dendrite length scale and interdendrite spacings. In order to produce a uniform microstructure, cooling from the molten state (T > 1100°C) is interrupted in the temperature of the semi-solid two-phase region (T~ 800-900°C) between the alloy liquidus and solidus temperature. The sample is held isothermally for several minutes in this region. The isothermal hold in the two-phase region allows the nucleation, growth, and coarsening of the ductile dendrite phase to approach thermodynamic equilibrium prior to final quenching. After the isothermal hold, the semi-solid mixture is cooled to vitrify the remaining liquid phase, and obtain a coarse and uniform dendrite distribution.

(3) The length scale of the dendritic phase is on the order of the length scale of deformation in the glass matrix. With softer dendrite phases deforming first and, subsequently initiating shear bands into the BMG matrix, interdendrite distance is limited to below a characteristic length scale [9, 10]. Matching of microstructural length scales to this characteristic length scale limits shear band extension, suppresses shear band opening, and avoids crack development. The composite

microstructure, with softer dendrites, creates short (stable) and dense shear bands rather than long (unstable) and sparse shear bands.

Details of material processing conditions can be found in Ref. 5.

5.3 Experimental (fracture property measurement)

Fracture toughness samples were prepared with various dimensions, limited by the lab-scale size of the water-cooled copper boat used to produce them. An initial notch was made in the middle of one side of the specimen using a wire saw. The diameter of the wire is ~ 170 μm. From the notched end, a pre-crack was generated by fatigue cracking with 5Hz of oscillating load (applied by an MTS hydraulic machine equipped with a 3 point bending fixture with adjustable span distance). The load level was kept at $\Delta K \cong 10 MPa \cdot m^{1/2}$, $K_{min}/K_{max} \cong 0.2$ and the pre-crack was generated until the crack length including the notch length, generated by the wire saw, reached half of the specimen width (45-55% of a specimen width). The pre-cracking process lasts approximately 40,000-100,000 cycles. With this pre-crack, a quasi-static compressive displacement of 0.3mm min^{-1} was applied and the load response of the pre-cracked sample was measured. Evaluation of J and of the J-R curve, by measuring unloading compliance and electrical resistance, were also performed during the test following the procedure described by ASTM E1820.

5.4 Basic concept for elastic and elastic-plastic fracture mechanics

The well known concept of Griffith energy balance was introduced in 1920. With an infinite plate under uniaxial tensile stress containing an interior sharp crack of 2a length (Figure

5-2), the conditions for crack growth will be determined by the following discussion; for an incremental increase in the crack area, potential (strain) energy decrease must be larger than the increase in surface energy by crack extension. This condition is expressed by Equation 5-1. Π, W_s and A refer to potential energy, surface energy and crack surface area, respectively.

$$\frac{dE}{dA} = \frac{d\Pi}{dA} + \frac{dW_S}{dA} = 0 \qquad \text{Equation 5-1.}$$

Potential (strain) energy can be defined as follows,

$$\Pi = \Pi_0 - \frac{\pi\sigma^2 a^2 B}{E} \qquad \text{Equation 5-2.}$$

Π_0 denotes potential (strain) energy of an uncracked plate. The strain energy released by the crack can be estimated by considering the release of strain energy a cylindrical element with diameter of crack length,2a, around the crack such that the energy release term is composed of the $\sigma^2/2E$ (strain energy per unit volume) and $\pi a^2 B$ (volume of cylindrical element around crack). With the formula for surface energy, $W_s=4aB\gamma_s$, Equation 5-1 gives the critical stress for crack growth in a brittle material (Equation 5-3) based on Griffith energy balance.

$$\sigma_f = \left(\frac{2E\gamma_S}{\pi a} \right)^{1/2} \qquad \text{Equation 5-3.}$$

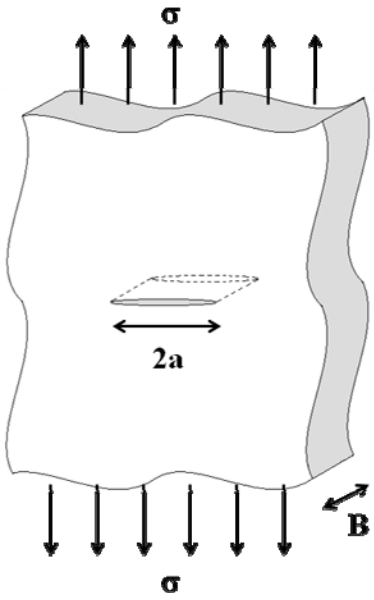

Figure 5-2. Infinite plate with interior crack for Griffith energy balance model.

In 1956, Irwin defined an energy release rate, G, which is a measure of the energy available for an increment of crack extension;

$$G = -\frac{d\Pi}{dA}$$ Equation 5-4.

The energy release rate (G) is the rate of change in potential energy with crack area. Since G is obtained from the derivative of a potential, it is also called the crack extension force or the crack driving force.

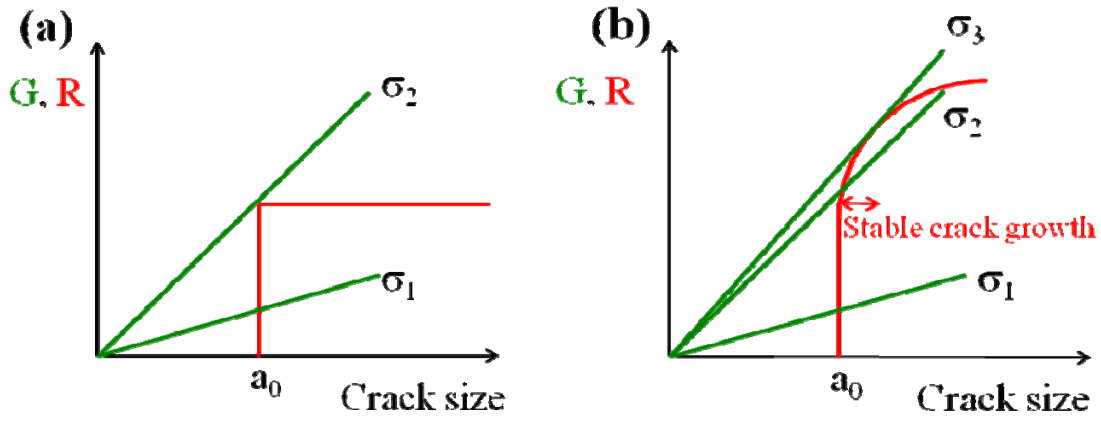

Figure 5-3. Simple resistance curve (R-curve) when (a) material resistance is constant with crack growth and (b) material has rising R-curve.

Figure 5-3 shows simplified fracture resistance curves. For a material having constant resistance with crack growth as shown in Figure 5-3(a), fracture occurs when the stress reaches σ_2. In this case, crack propagation is unstable because the driving force increases with crack growth, but the material resistance remains constant. On the other hand, Figure 5-3(b) shows a rising resistance curve. The crack starts growing when the stress reaches σ_2, but cannot grow further unless the stress increases. Instability occurs when the stress reaches σ_3.

In 1960, Rice introduced a path-independent contour integral for analysis of cracks. He then showed that the value of this integral, which he called J, is equal to the energy release rate (G) in a nonlinear elastic body that contains a crack. Laboratory measurement of J for a growing crack is defined by ASTM E1820. Figure 5-4 shows a typical J-R curve for a ductile material. During loading, crack blunting occurs at the early stage, and the crack starts growing at a critical point. J_{IC} is defined near the initiation of stable crack growth, but it is difficult to define the exact initiation point as in the case of yield stress of tensile testing. Therefore, a 0.2mm offset method

like a 0.2% offset yield stress is used for J_{IC} determination. Initiation toughness (J_{IC}) is important, but it should be also noted that the entire R curve gives a more complete description of fracture behavior.

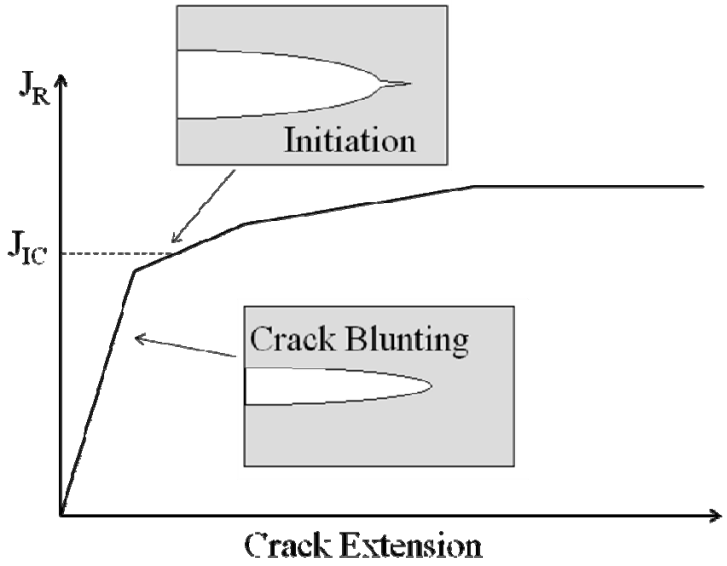

Figure 5-4. Typical J-R curve for a ductile material.

5.5 Load-displacement behavior of composites with different compositions

Figure 5-5 shows load-displacement curves of composites with different compositions. They look different from a typical load-displacement curve of a monolithic BMG introduced in Figure 5-1. Physical properties of these alloys are given in Table 5-1 [5]. The alloy $Zr_{36.6}Ti_{31.4}Nb_7Cu_{5.9}Be_{19.1}$ (DH1) still shows unstable (abrupt) crack propagation behavior, but $Zr_{38.3}Ti_{32.9}Nb_{7.3}Cu_{6.2}Be_{15.3}$ (DH2) and $Zr_{39.6}Ti_{33.9}Nb_{7.6}Cu_{6.4}Be_{12.5}$ (DH3) are different. The curves start to bend over when K= 55-73 $MPa{\cdot}m^{1/2}$, but they appear to have stable crack growth and

clearly have absorbed a large amount of energy. Thus, it is reasonable to consider different fracture parameter such as energy terms rather than the stress term, like stress intensity factor (K). A simple calculation of energy consumption for crack growth gives a rough idea of resistance of each composite against crack growth. As given in Table 5-2, overall energies dissipated during crack propagation process are 0.60, 1.06 and 1.38 Joules for DH 1, 2 and 3, respectively. Dividing these energy values by the areas of newly generated cracks (amount of crack propagation, 3.0, 2.3 and 1.6 mm) yields energy consumed per unit area of fracture surface, G = 77, 178 and 341 kJ/m^2. Although these are rough estimations, simple conversion to stress intensity factor (K) using relation for plane strain condition, $G= K^2/E \times(1-\nu^2)$, and elastic properties given in Table 5-1 calculates K values of 87, 124 and 173 $MPa \cdot m^{1/2}$, respectively. This estimation is not rigorous because it does not differentiate crack initiation stage from crack propagation stage. Moreover, the plane strain condition is not satisfied here, due to limitations in the sample's thicknesses, which will be discussed later. Nevertheless, the fracture behavior of DH 1, 2 and 3 composite alloys shows the clear toughening effect of the ductile dendrite phase.

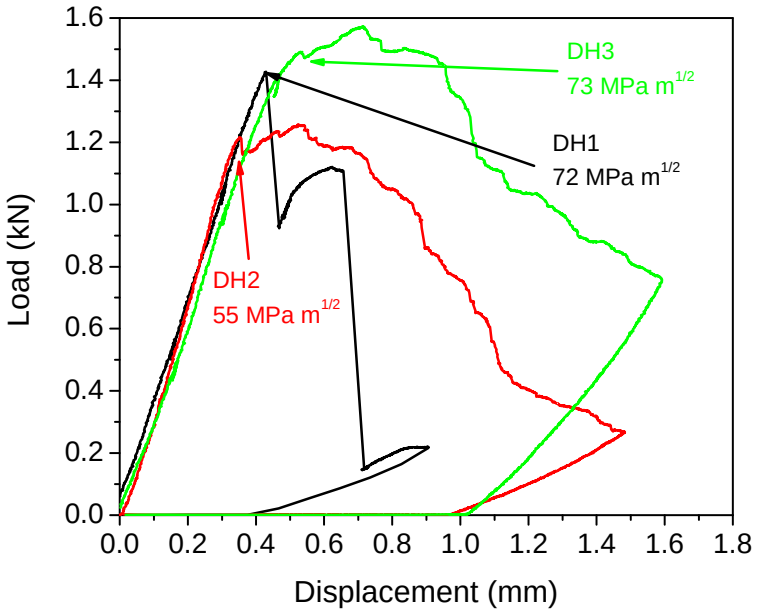

Figure 5-5. Load-displacement curves of composites with different compositions.

Table 5-1. Physical properties of different composites [5]. Dendrite volume fraction, yield stress, Young's modulus and Poisson's ratio.

Alloy	Dend. vol. frac. (%)	σ_y (MPa)	E (GPa)	ν
DH1 ($Zr_{36.6}Ti_{31.4}Nb_7Cu_{5.9}Be_{19.1}$)	42	1474	84.3	0.371
DH2 ($Zr_{38.3}Ti_{32.9}Nb_{7.3}Cu_{6.2}Be_{15.3}$)	51	1367	79.2	0.373
DH3 ($Zr_{39.6}Ti_{33.9}Nb_{7.6}Cu_{6.4}Be_{12.5}$)	67	1096	75.3	0.376

Table 5-2. Dimensions of fracture test specimens and fracture test results.

a_0 denotes initial pre-crack length (notch + pre-crack).

Typical 3-pt bending specimen is illustrated in Figure 3-1.

G = (Area of load-disp. curve)/(thick × Δa) and $G = K^2/E \times (1-\nu^2)$.

Alloy	thick (mm)	a_0 (mm)	width (mm)	span (mm)	Area of load-disp. curve (J)	crack extension Δa (mm)	G (kJ/m^2)	K ($MPa \cdot m^{1/2}$)
DH1 ($Zr_{36.6}Ti_{31.4}Nb_7Cu_{5.9}Be_{19.1}$)	2.58	4.5	8.3	31.75	0.6	3	77	87
DH2 ($Zr_{38.3}Ti_{32.9}Nb_{7.3}Cu_{6.2}Be_{15.3}$)	2.63	3.8	7.8	31.75	1.06	2.3	178	124
DH3 ($Zr_{39.6}Ti_{33.9}Nb_{7.6}Cu_{6.4}Be_{12.5}$)	2.5	4.4	8.3	31.75	1.38	1.6	341	173

5.6 Comparison of two composites with different compositions

5.6.1 Crack growth estimation by unloading compliance

$Zr_{39.6}Ti_{33.9}Nb_{7.6}Cu_{6.4}Be_{12.5}$ (DH3) and $Zr_{37.5}Ti_{32.2}Nb_{7.2}Cu_{6.1}Be_{17}$, an alloy with a composition that falls in between DH1 and DH2 (this alloy is denoted as DH2* hereafter), are compared. DH1-3 alloys are designed based on the formula $(Zr_{45.2}Ti_{38.8}Ni_{8.7}Cu_{7.3})_{100-X}Be_X$ with x=19.1, 15.3 and 12.5 for DH1, DH2 and DH3, respectively. As the Be content, x, decreases, one obtains an increasing volume (or molar) fraction of dendrite phase in a glass matrix, as shown in Table 5-1. DH1-3 alloys partition by volume fraction into 42%, 51% and 67% dendritic phase in a glass matrix, respectively [5]. DH2* has x=17, which places in between 15.3 and 19.1. Therefore, DH2* is expected to have a dendrite fraction between 42 and 51%.

Since the fracture properties estimated by the overall energy consumption cannot differentiate different stages of crack initiation and propagation, it is necessary to monitor the crack growth behavior (position of the crack tip or crack length) during loading. Practical and well known methods are ‘unloading compliance’ and ‘potential drop’ methods [11]. The

'unloading compliance' method was used for this discussion and 'potential drop' method using typical 4-point probe electrical resistance measurement will be used and discussed in the latter part of this chapter. Unloading lines are used for estimating 'crack length' based on the formula given by ASTM E1820 (section A1.4.3):

$$a/W = 0.999748 - 3.9504u + 2.9821u^2 - 3.21408u^3 + 51.51564u^4 - 113.031u^5$$

Equation 5-5.

where :

$$u = \frac{1}{\left[\frac{BWEC}{S/4}\right]^{1/2} + 1}$$

Equation 5-6.

$C = (\Delta v_m/\Delta P)$ on an unloading/reloading sequence,

v_m= crack opening displacement at notched edge (in this study, ram displacement is used instead of crack opening displacement).

a = crack length, B = specimen thickness, W = specimen width, E = Young's modulus, and S = span distance of 3-pt bending fixture.

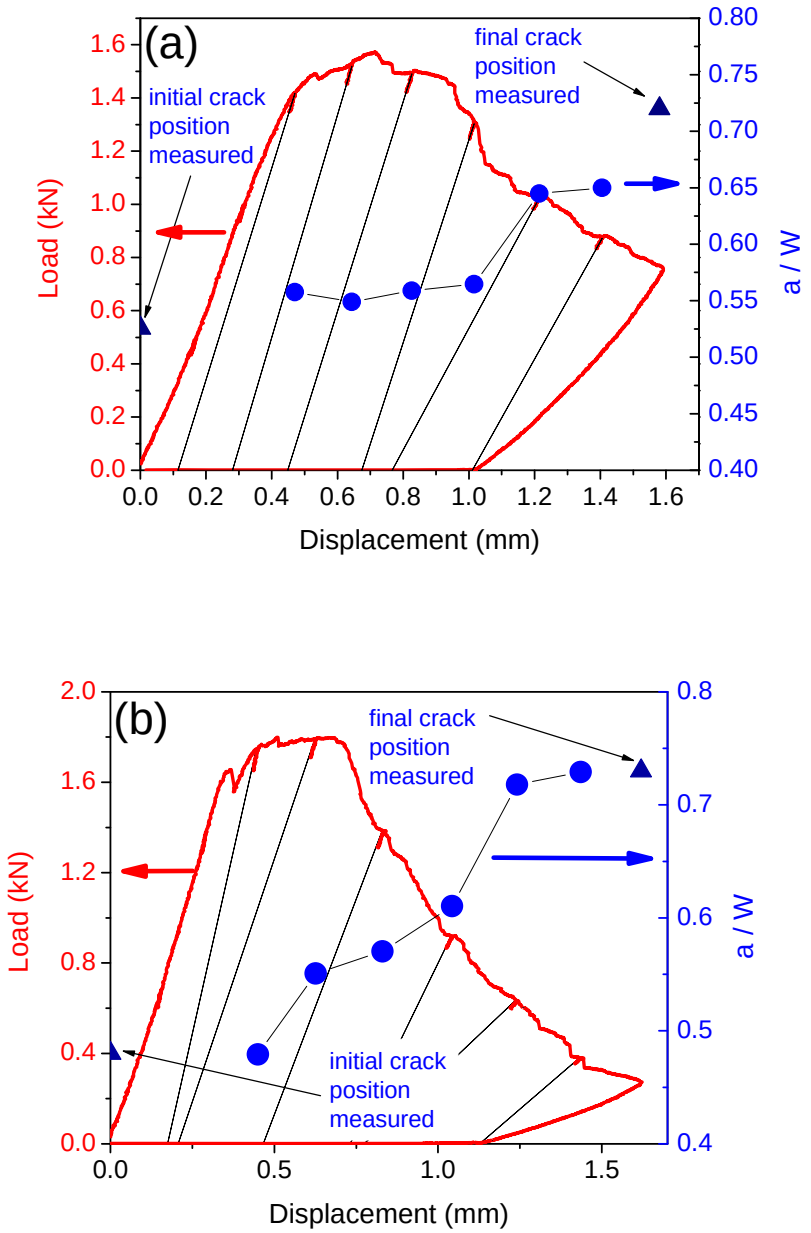

Figure 5-6. Crack length estimation by unloading compliance on (a) DH3 and (b) DH2*. Triangles show crack position measured before and after fracture test.

Figure 5-6 shows results of crack length estimation using the formula given by Equation 5-5 and 5-6. Compared to the actual crack propagation measured before and after fracture test (shown by triangles in the figures), it underestimates the crack propagation of DH3 as shown in Figure 5-6(a), but shows relatively good agreement for DH2* specimen shown in Figure 5-6(b).

The slopes of unloading lines decrease as the crack front advances. A prominent difference between these two specimens is the initiation of slope change. The slope of DH3 starts decreasing later than DH2* does which implies that the crack starts to grow much later than the bending-over point in load-displacement curve in DH3. Since it appears that the bending-over of the load-displacement curve is not from crack advancing but from crack blunting, elastic-plastic fracture mechanics is required to characterize the fracture behavior of these composites. Although the number of unloading lines used for these specimens are not enough to satisfy ASTM 1820 for J-R curve method, a rough estimation of initiation J_Q (J_{IC} in case of plane strain condition) using this unloading compliance method gives ~≥260 kJ/m^2 for DH3 and ~120 kJ/m^2 for DH2*, which can be converted to stress intensity factor (K) for comparison purpose, K~≥ 151 and ~105 MPa·m$^{1/2}$, respectively. These numbers are similar to the numbers calculated from the concept of overall energy consumption. In order to confirm the high toughness of the composites, a more refined evaluation of J is necessary.

5.6.2 Difference in the microstructure

Microstructures of both specimens also agree with the observation stated above. Figure 5-7 compares low magnification images of two fractured specimens: DH3 and DH2*. It is clear that the crack advances more in DH2* than in DH3. Figure 5-8 shows areas where the advancing cracks are arrested (indicated by an arrow on the top of each image). Heavy deformation around

the crack appears to make the specimen's surface look significantly rough. Apparently, the microstructure of DH2* (Figure 5-8(b)) has larger dendrites and larger interdendrite spacing. Small crack openings are also observed in DH2*, which are not observed in DH3. The difference looks more apparent in Figure 5-9. Both Figure 5-9(a) and (b) look almost identical in dendrite size and interdendrite spacing, but they have different magnification: 6000× for DH3 in Figure 5-9(a) and 3000× for DH2* in (b). So the shear bands in DH2* run about twice as far as those in DH3 specimen. Moreover, a shear band located on center of Figure 5-9(b) runs particularly longer than the others and appears to develop into a crack. This observation is fairly consistent with the designing strategy, "matching characteristic length scale", introduced by Hofmann et al. [5].

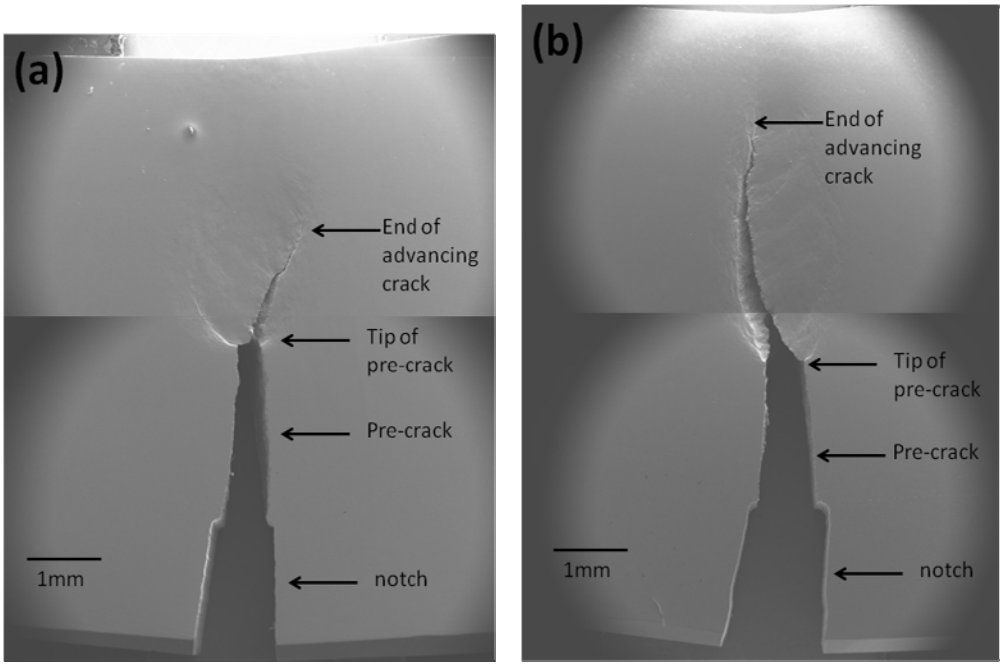

Figure 5-7. Low magnification images of fracture specimens. (a) DH3 and (b) DH2*.

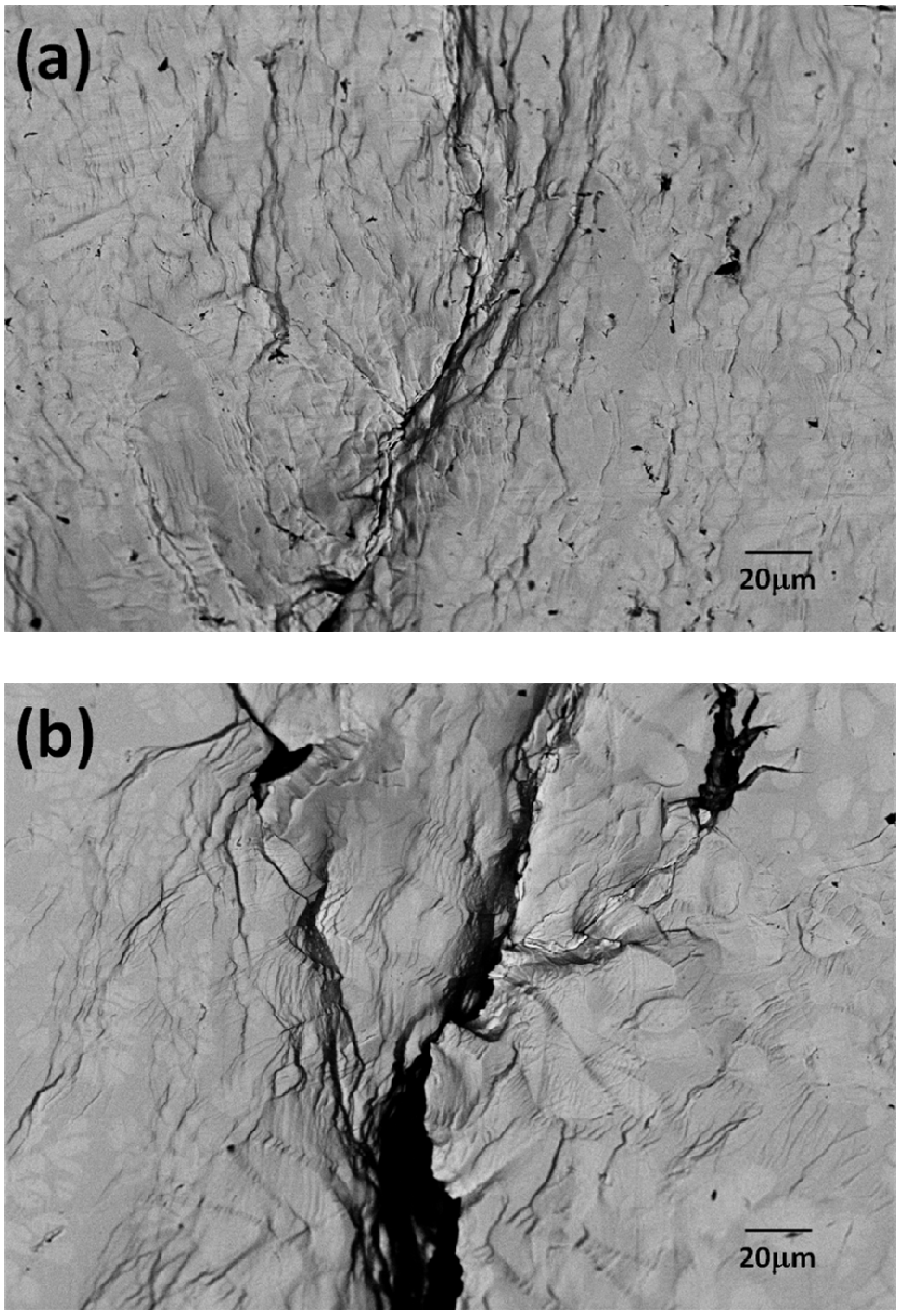

Figure 5-8. Back-scattered electron images of the surfaces of fracture specimens near the crack arresting point. (a) DH3 and (b) DH2*. Both images are taken by 1000× magnification.

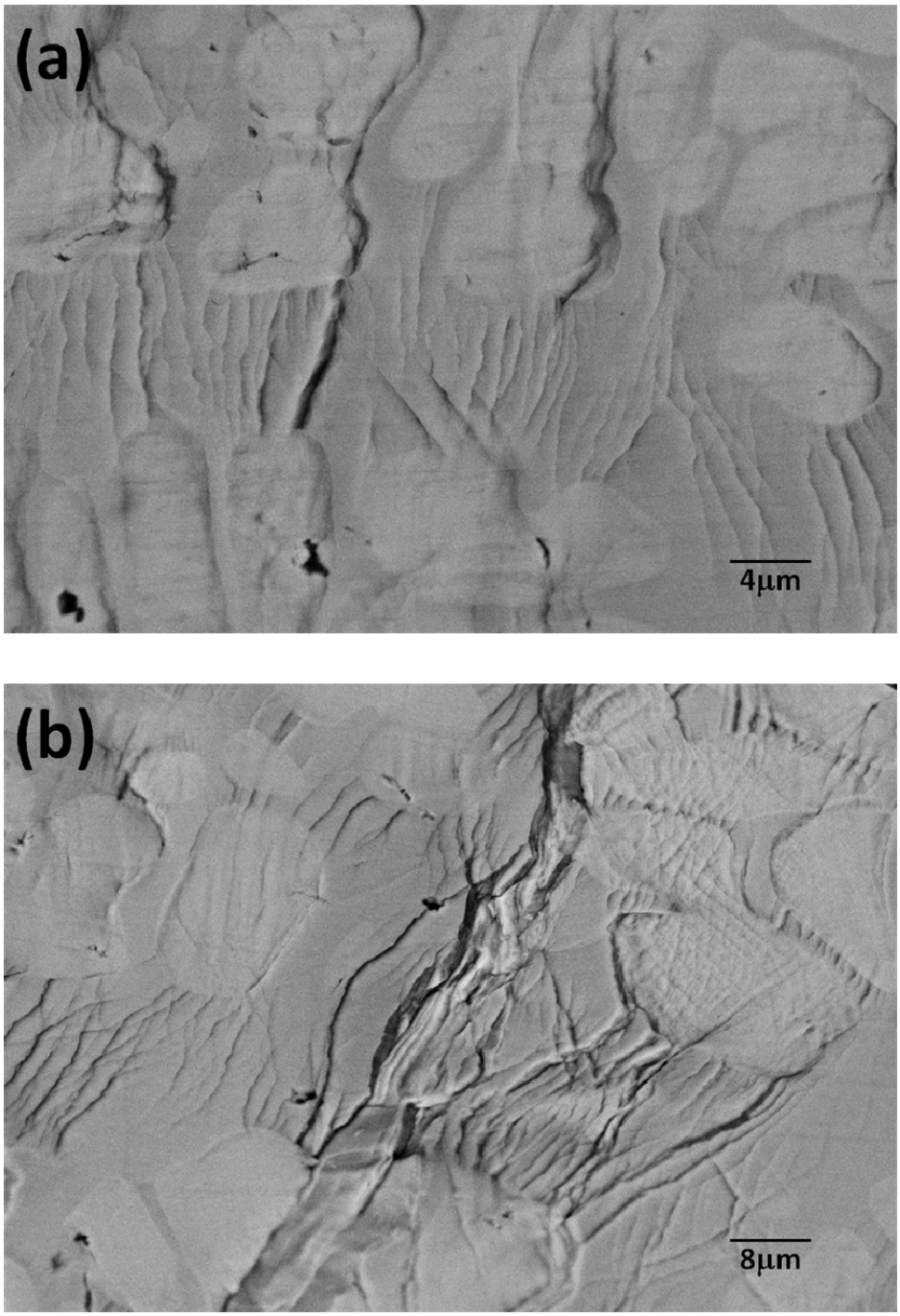

Figure 5-9. Magnified back-scattered electron images of the surfaces of fracture specimens near crack arresting point. (a) DH3 with 6000× magnification and (b) DH2* with 3000× magnification.

5.7 J-R curve evaluation with thicker specimens

It is apparent that the fracture tests performed above do not satisfy the standard requirement for specimen size. However, the current equipment for material production limits specimen size to below 5 mm in thickness. (A new setup for larger specimen production has been completed recently and additional fracture toughness evaluation is ongoing by a fracture mechanics research group in Lawrence Berkeley Laboratory.) Although the current 5 mm thickness is not enough to support a case that the material has fracture toughness of 170 $MPa \cdot m^{1/2}$, it's still worth exploring the fracture toughness of specimens with varying thicknesses. In addition to the 2.5 mm thick specimen measured above, 4.18, 4.86 and 5.21 mm thick specimens of DH3 ($Zr_{39.6}Ti_{33.9}Nb_{7.6}Cu_{6.4}Be_{12.5}$) have been evaluated. Both 4.18 and 4.86 mm thick specimens have been prepared by arc-melting and semi-solid processing in a copper boat, but due to the size limitation of the copper boat equipment, a 5.21 mm thick specimen was created directly from the arc-melter, without additional processing.

J-R curve measurement for these specimens is performed following the guideline given by the ASTM standard. As a verification tool for the crack length estimation by unloading compliance, electrical resistance measurement (potential drop) is utilized. Electrical resistance increases as cracks grow since the crack growth reduces the effective area through which electric current flows. Figure 5-10 shows a schematic diagram of potential drop measurement.

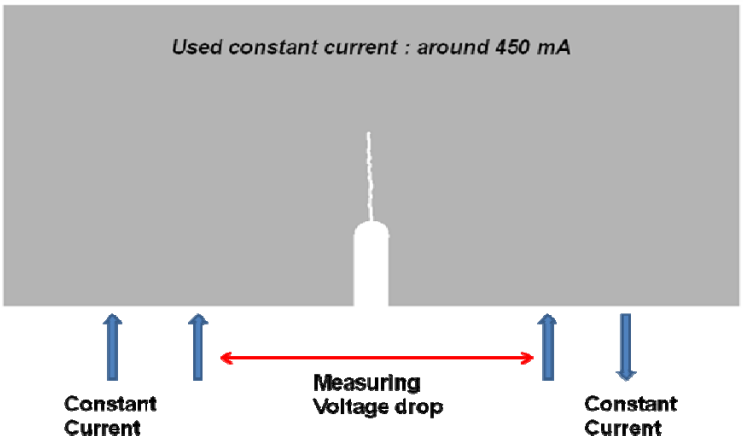

Figure 5-10. Potential drop (electrical resistance) measurement setup for fracture specimen.

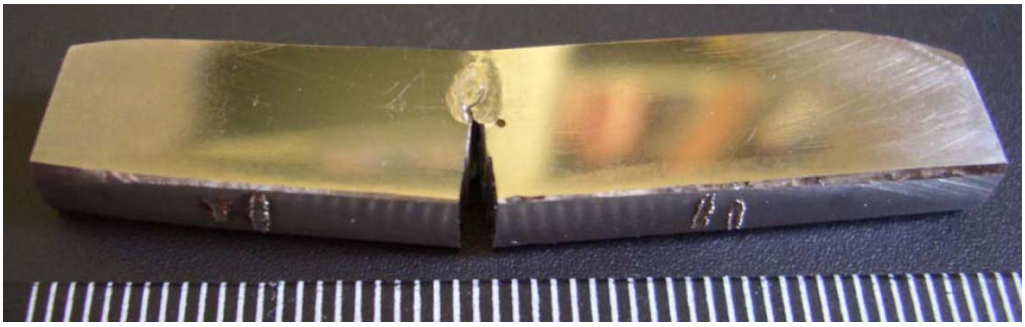

Figure 5-11. 5.21 mm thick specimen of DH3 ($Zr_{39.6}Ti_{33.9}Nb_{7.6}Cu_{6.4}Be_{12.5}$) after test.

5.7.1 Evaluation procedure for 5.21 mm thick specimen

Figure 5-11 shows the overall deformation of a 5.21 mm thick specimen of DH3 ($Zr_{39.6}Ti_{33.9}Nb_{7.6}Cu_{6.4}Be_{12.5}$) after fracture testing. The specimen width (W) was 9.3 mm and initial crack length (a_0) was 4.85 mm, thus the initial ligament size was $b_0 = W-a_0 = 9.3-4.85 = 4.45$ mm. The span distance for the 3-pt bending fixture is 38.1 mm. This specimen is too thick for the copper boat so semi-solid processing was not done. In other words, this is a specimen directly

from the arc-melter. As shown in Figure 5-11, about 2 mm of crack opening is obtained by the fracture test and large area of plastic zone is observed. It should be noted that, in spite of the large amount of deflection in this specimen, the crack advanced only about 2.5 mm before stopping.

Figure 5-12 is a load-displacement curve with unloading lines. The slope of the unloading lines decreases as the crack advances. In Figure 5-13, the crack position estimated by unloading compliance is shown by a curve connected with circles and voltage drop through the specimen under constant current flow is shown by a line. Crack length curves acquired by unloading compliance method and voltage drop method appear identical in shape. Additionally, the estimated crack position is close to the numbers measured by calipers before and after the test, which are shown by triangles in the plot. Therefore, it is reasonable to use these estimated numbers for the following J-calculation.

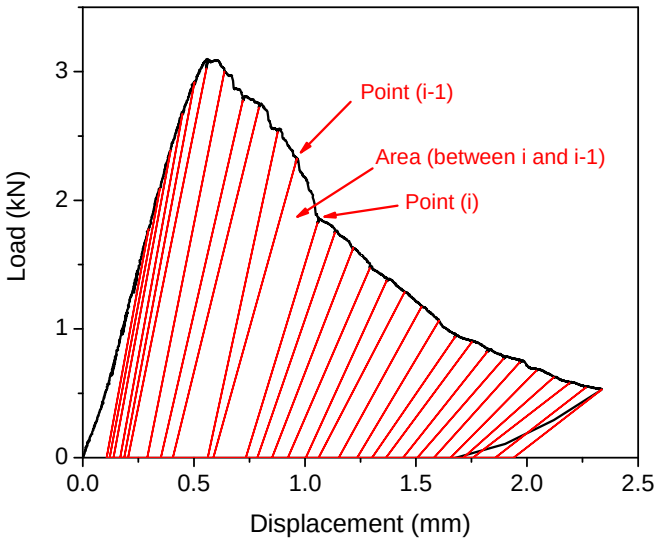

Figure 5-12. Load-displacement curve and unloading compliance lines from 5.21 mm thick specimen.

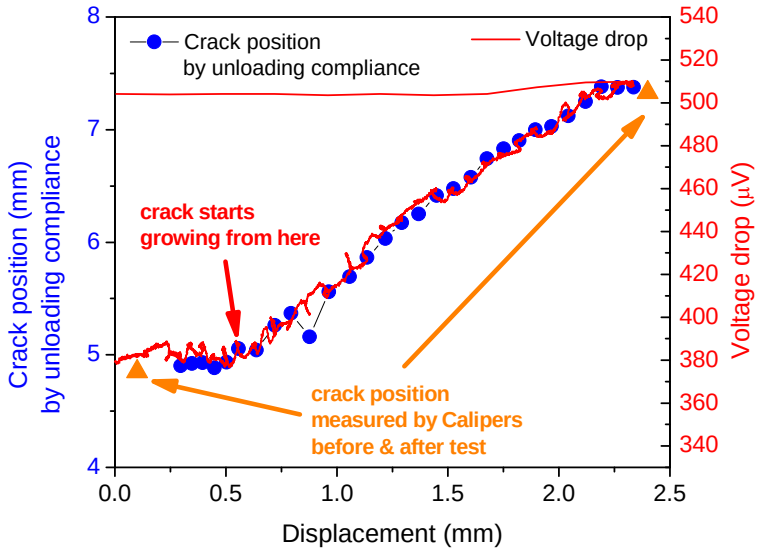

Figure 5-13. Crack position estimation by unloading compliance which is agreeing with crack position before and after test measured by calipers and potential drop line in overall shape.

Using the incremental formula given by Equations 5-7, 8 and 9, elastic and plastic component of the J parameter is calculated. Definitions of point (i) and point (i-1) are given in Figure 5-12.

$$J_{(i)} = J_{elastic\,(i)} + J_{plastic\,(i)}$$ Equation 5-7.

$$J_{elastic\,(i)} = \frac{\left(K_{(i)}\right)^2\left(1-\nu^2\right)}{E}$$ Equation 5-8.

$$J_{plastic\,(i)} = \left[J_{plastic\,(i-1)} + \left(\frac{2}{w-a_{(i-1)}} \right)\left(\frac{Area(between\ \ i\ and\ i-1)}{B} \right) \right] \cdot \left[\frac{w-a_{(i)}}{w-a_{(i-1)}} \right]$$

Equation 5-9.

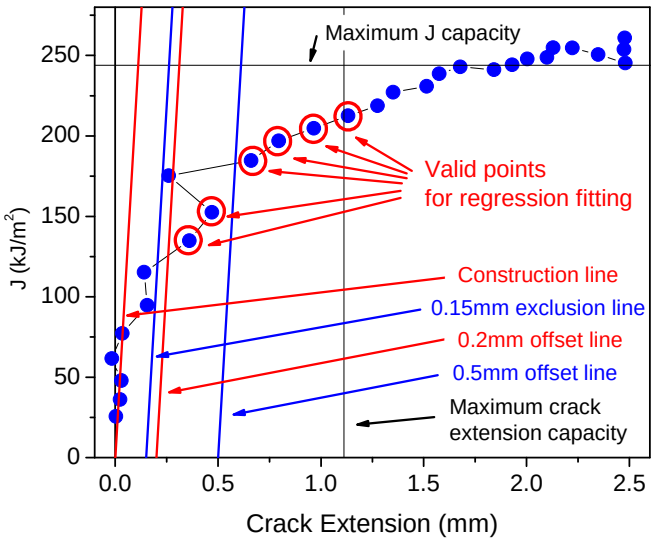

Figure 5-14. J-R curve for 5.21 mm thick specimen.

The calculated J parameter is plotted in Figure 5-14 as a function of crack extension ($\Delta a = a - a_0$).The following conditions limit the validity of J-R curve acquired.

(1) The unload/reload sequences should be spaced with the displacement interval not to exceed 0.01 W. This condition is satisfied for this specimen and the following 4.18 and 4.86 mm thick specimens.

(2) The maximum J-integral capacity for a specimen is given by the smaller of the following:

$$J_{max} = \frac{b\sigma_Y}{20} \quad \text{or} \quad \text{Equation 5-10.}$$

$$J_{max} = \frac{B\sigma_Y}{20} \quad \text{Equation 5-11.}$$

For this specimen, Equation 5-10 applies with J_{max} = 244 kJ/m^2 (indicated in Figure 5-14).

(3) The maximum crack extension capacity for a specimen is given by the following Equation 5-12.

$$\Delta a_{\max} = 0.25 \cdot b_0 \qquad \text{Equation 5-12.}$$

The maximum crack extension capacity for this specimen is 1.11 mm (shown in Figure 5-14).

With the restrictions given above, the following procedure is taken to determine J_Q using the acquired J-R curve shown in Figure 5-14.

(1) Plot a construction line in accordance with the following equation: (plotted in Figure 5-14)

$$J = 2\,\sigma_Y\,\Delta a \qquad \text{Equation 5-13.}$$

(2) Then draw an exclusion line parallel to the construction line intersecting the abscissa at 0.15 mm (drawn in Figure 5-14). Draw a second exclusion line parallel to the construction line intersecting the abscissa at 1.5 mm. This 1.5 mm exclusion line is not shown in Figure 5-14 because Δa_{max} (= 1.11 mm) is less than 1.5 mm. Data points that don't fall inside the area enclosed by these two exclusion lines capped by J_{max} (Equation 5-10 or 11) should be thrown away.

(3) At least one point shall lie between the 0.15 mm exclusion line and a parallel line with an offset of 0.5 mm from the construction line. The 5.21 mm thick specimen has 2 points in this region (Figure 5-14).

(4) At least one point shall lie between this 0.5 mm offset line and 1.5 mm exclusion line. The 5.21 mm thick specimen has 4 points in this region (Figure 5-14).

(5) Using the data points which conform to the requirement stated above (6 data points for this specimen), determine a linear regression line of the following form:

$$\ln J = \ln C_1 + C_2 \ln\left(\frac{\Delta a}{k}\right)$$ Equation 5-14.

where k=1.0 mm.

(6) The intersection of the regression line (Equation 5-14) with the 0.2 mm offset line defines J_Q.

122.2 kJ/m^2 is acquired for this specimen as shown in Figure 5-15.

Qualification of J_Q as J_{IC}, a size independent value of fracture toughness, requires following three conditions to satisfy.

(1) Thickness B > 25 J_Q/σ_Y.

For this specimen, 25 J_Q/σ_Y = 2.79 mm, and the specimen thickness 5.21 mm is larger than 2.79 mm, thus this condition is satisfied.

(2) Initial ligament, b_0 > 25 J_Q/σ_Y.

Initial ligament size, 4.45 mm is also larger than 2.79 mm, thus this condition is satisfied.

(3) Regression line slope – the slope of the power law regression line, dJ/da, evaluated at Δa_Q should be less than σ_Y. For this specimen, slope of regression line at Δa_Q is 187 MPa which is smaller than σ_Y, 1096 MPa. This condition is satisfied.

Therefore, the measured J_Q can be regarded as J_{IC}: J_{IC} = 122.2 kJ/m^2. And, the stress intensity factor converted from J_{IC} is, K_{JIC} = 103.5 MPa·m$^{1/2}$.

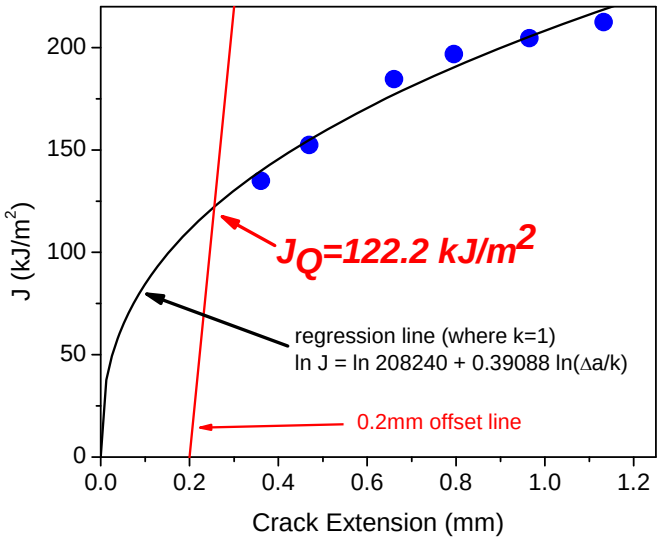

Figure 5-15. Regression curve fitting for J_Q determination of 5.21 mm thick specimen.

5.7.2 Evaluation with 4.18 and 4.86 mm thick specimens

Figure 5-16 shows an overall image of 4.18 and 4.86 mm thick DH3 ($Zr_{39.6}Ti_{33.9}Nb_{7.6}Cu_{6.4}Be_{12.5}$) specimens after testing. Both specimens are prepared by arc-melting and semi-solid processing in a copper boat. The 4.18 mm thick specimen has 34.925 mm of span distance (S), 9.19 mm of specimen width (W) and 4.30 mm of initial crack length (a_0). For this sample, S = 38.1 mm, W= 9.38 mm and a_0 = 5.13 mm. About 2 mm of crack opening is obtained by each fracture test and a large area of plastic zone is observed like that of the 5.21 mm thick specimen. The cracks advance only about 1.8 and 1.5 mm, respectively for the 4.18 and 4.86 mm thick specimens.

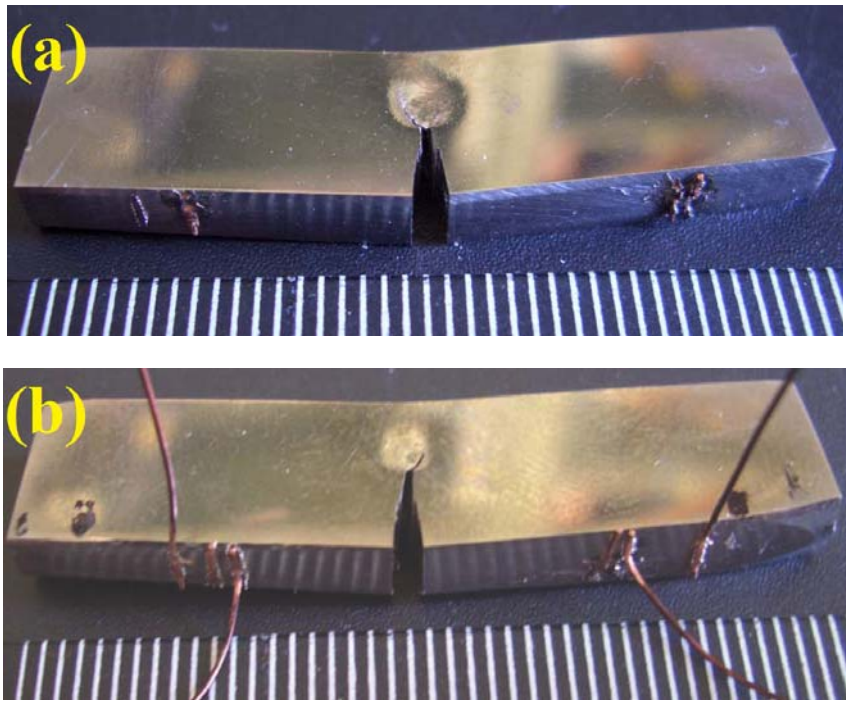

Figure 5-16. (a) 4.18 and (b) 4.86 mm thick DH3 ($Zr_{39.6}Ti_{33.9}Nb_{7.6}Cu_{6.4}Be_{12.5}$) specimens after testing.

Crack length curves acquired by the unloading compliance method and voltage drop method look identical in overall shape, as shown in Figure 5-17. Additionally, the estimated crack positions are close to the numbers measured by calipers before and after test.

J-R curves are shown in Figure 5-18 for both specimens. Due to the extensive deformation before crack extension, J curves show a steep increase passing the maximum J capacity (J_{max}) at the early stage of deformation. J_{max} is defined to be 229 and 266 kJ/m^2 for the 4.18 and 4.86 mm thick specimens, respectively. The critical J (J_Q) may be approximated by intersecting point with 0.2 mm offset line: 326 and 321 kJ/m^2. These two J_Q values are almost identical and represent 170 and 168 MPa·m$^{1/2}$ of stress intensity factors. But, these are not valid numbers for standard plane strain J_{IC}.

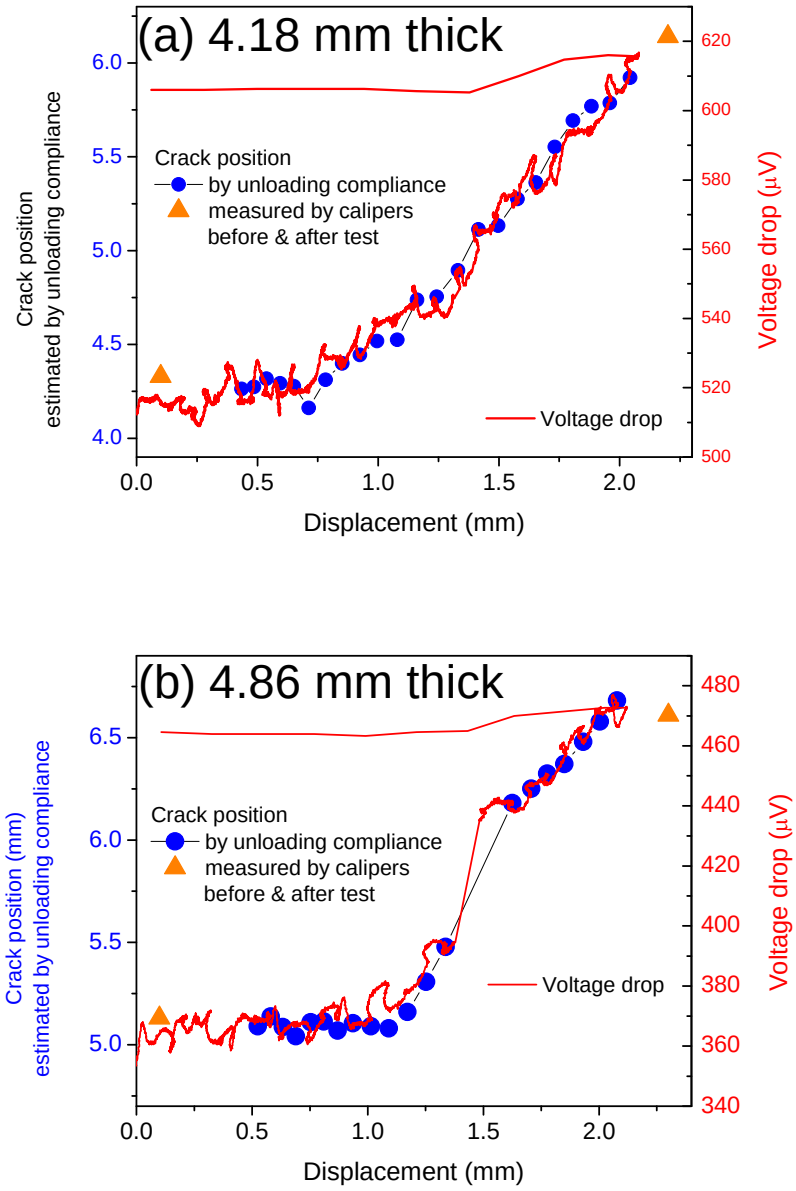

Figure 5-17. Crack position estimation for (a) 4.18 and (b) 4.86 mm thick specimens by unloading compliance which agrees with crack position before and after the test, as measured by calipers and potential drop line in overall shape.

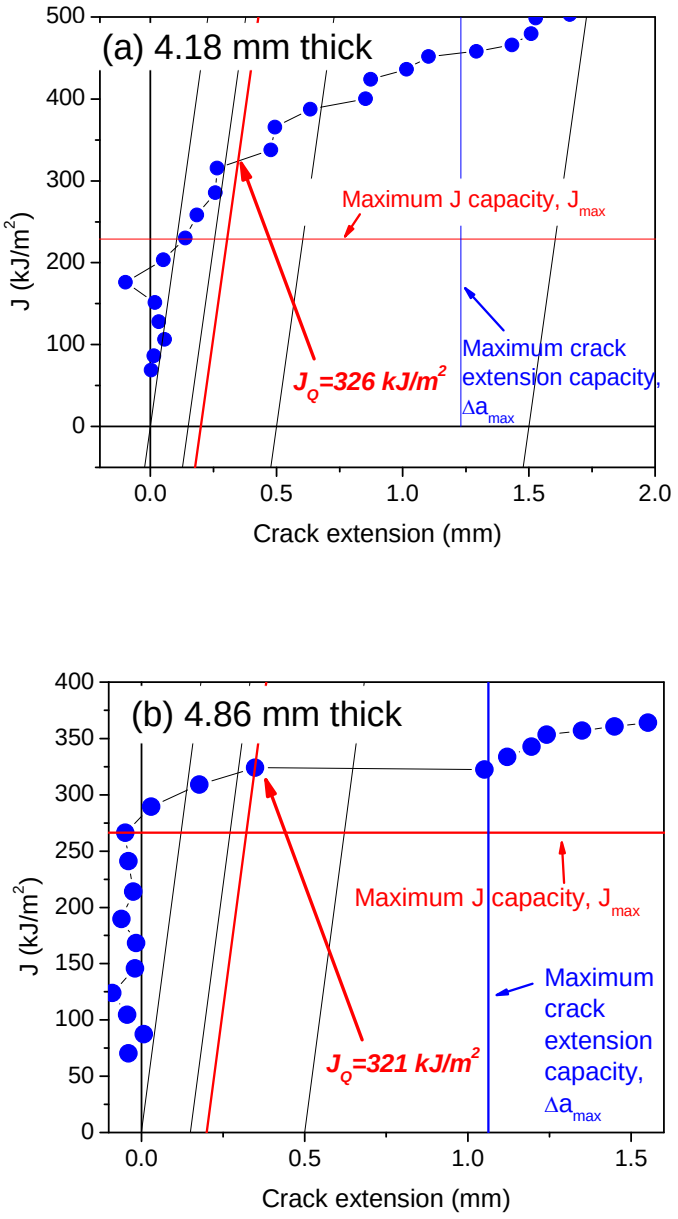

Figure 5-18. J-R curve for (a) 4.18 and (b) 4.86 mm thick specimens.

5.7.3 Effect of semi-solid processing

Load-displacement curves of DH3 ($Zr_{39.6}Ti_{33.9}Nb_{7.6}Cu_{6.4}Be_{12.5}$) specimens with different thickness are compared in Figure 5-19. As pointed out earlier, the 5.21 mm thick specimen is machined directly from an arc-melted ingot. The others are prepared by arc-melting and semi-solid processing in a copper boat. It is important to notice that the 5.21 mm thick specimen does not show a 'flat' area around the maximum load point. Unlike the others, the load-displacement curve of the 5.21 mm thick specimen starts decreasing right after it reaches maximum point. It appears that the 'flat' region of load-displacement curve is due to the heavy plastic deformation around crack tip area rather than crack growth. Crack growth induces a steeper decrease of the load-displacement curve.

The earlier composites without semi-solid processing [1,2] had cooling rate dependent microstructure and likely had large variations in the overall dendrite length scale and interdendrite spacings. The aim of semi-solid processing is to fully develop the microstructure and homogenize it. Compared to other compositions, like DH1 and 2, DH3 ($Zr_{39.6}Ti_{33.9}Nb_{7.6}Cu_{6.4}Be_{12.5}$) has higher volume fraction of ductile dendrite phase. With fully developed dendrite structure, DH3 has the minimum interdendrite distance among the three different compositions. This interdendrite distance of DH3 appears to match the characteristic length scale so that shear band extension is limited and transition into a crack is prohibited while the metallic glass part, comprising a significant fraction of the whole material, keeps the strength unusually high. Without semi-solid processing, there is no guarantee of uniform microstructure. Even with the composition of DH3, an undeveloped microstructure can cause transition of shear bands into cracks at the early stages of deformation as shown in Figure 5-9(b).

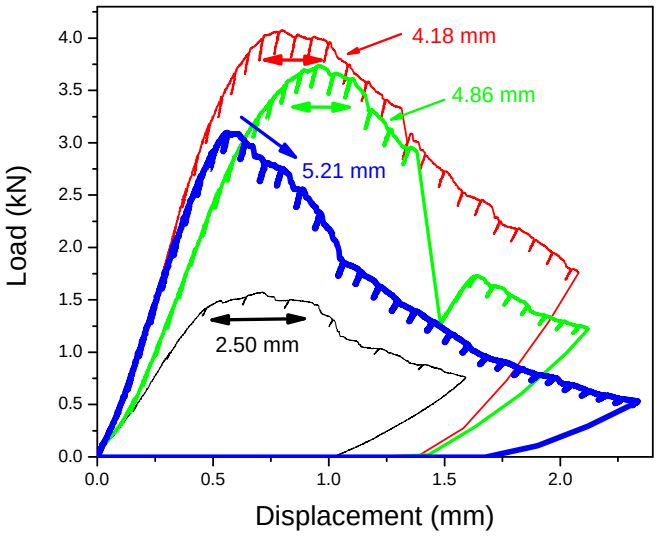

Figure 5-19. Load-displacement curves of four specimens with different thicknesses.

5.7.4 Effect of specimen thickness

Figure 5-20 shows four data points of fracture toughness expressed in terms of stress intensity factor. The curved line defines the dimensional restriction for valid fracture toughness given for a specific stress intensity factor (K) calculated from B, $b_0 > 25\ J_Q/\sigma_Y$ and a relation between energy term and stress intensity factor, $G= K^2/E \times(1-\nu^2)$. The relation means that, for a given converted stress intensity factor to be regarded as an outcome of a valid J_{IC} measurement, both thickness and ligament size ($b_0 = W – a_0$) of a fracture specimen have to be larger than a number defined by this curve. In other words, the data points should be located to right of the curve in Figure 5-20. According to the curve, the 4.86 mm thick specimen is valid for a measurement of fracture toughness up to 136 MPa·$m^{1/2}$. On the other hand, in order to measure a valid fracture toughness of 170 MPa·$m^{1/2}$, a sample thickness of at least 7.5 mm is needed. However, based on the information currently available, the critical value (J_Q) does not seem to be

affected by the specimen thickness. Although J_Q could possibly decrease rapidly at higher thicknesses, the trend seems to be along the extrapolation line given in Figure 5-20. This will be reinvestigated when new equipment with larger material production capacity becomes available.

It should be noted that even when the material is not semi-solidly processed, K_{JIC} is still as high as 104 MPa·$m^{1/2}$. Since it is known that tensile ductility goes from ~3% to ~13% with semi-solid processing [5], it makes sense that K_{IC} increases as well.

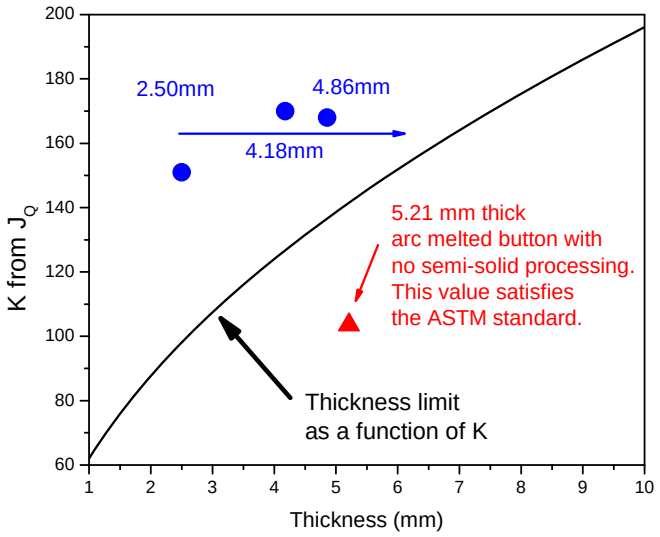

Figure 5-20. Fracture data of four specimens with different thickness expressed in stress intensity factor (K) and a curve showing limitations of specimen dimension for valid J_{IC} evaluation.

5.8 Conclusion

Unlike monolithic BMG's, BMG composites show stable crack growth and crack arrest. Enhanced fracture properties of the composite can be attributed to earlier deformation of the

ductile phase, subsequent activation of shear bands in the BMG matrix and confinement of those shear bands to keep them from developing into cracks. Increasing the volume fraction of ductile dendrite phase with fully developed microstructure increases amount of energy needed to advance existing cracks. This tendency is consistent with the designing concept of “matching the characteristic length scale”.

J-R curve evaluation of the composites reveals significant improvement in fracture toughness, having values perhaps larger than 136 $MPa \cdot m^{1/2}$. Current efforts to improve specimen production will provide a full understanding of fracture behavior of the composites and standard J_{IC} and K_{JIC} values.

Acknowledgements

The authors would like to thank Prof. G. Ravichandran of GALCIT, Caltech for providing theh MTS test system. This work was supported in part by the MRSEC Program of the National Science Foundation under Award Number DMR-0520565. We also acknowledge the Office of Naval Research for partial support of this work.

References

[1] C.C. Hays, C.P. Kim and W.L. Johnson, Phys. Rev. Lett. 84 (2000) 2901.

[2] F. Szuecs, C.P. Kim and W.L. Johnson, Acta Mater. 49 (2001) 1507.

[3] K.M. Flores, W.L. Johnson and R.H. Dauskardt, Scripta Mater. 49 (2003) 1181.

[4] G. Duan, A. Wiest, M.L. Lind, J. Li, W.-K. Rhim and W.L. Johnson, Adv. Mater. 19 (2007) 4272.

[5] D.C. Hofmann, J.-Y. Suh, A. Wiest, G. Duan, M.L. Lind, M.D. Demetriou and W.L. Johnson, Nature 451 (2008) 1085.

[6] D.C. Hofmann, J.-Y. Suh, A. Wiest and W. Johnson, Scripta Mater. 59 (2008) 684.

[7] R.D. Conner, W.L. Johnson, Scripta Mater. 55 (2006) 645.

[8] C.P. Kim, J.-Y. Suh, A. Wiest, M.L. Lind, R.D. Conner and W.L. Johnson, Scripta Mater. 60 (2008) 80.

[9] R.D. Conner, W.L. Johnson, N.E. Paton and W.D. Nix, J. Appl. Phys. 94(2) (2003) 904.

[10] R.D. Conner, Y. Li, W.D. Nix and W.L. Johnson, Acta Mater. 52 (2004) 2429.

[11] T.L. Anderson, Fracture Mechanics: Fundamentals and Applications, 1st ed. (CRC Press, 1991) p.425.

Appendix 5-A Machine compliance correction for MTS test machine

It is important to have this additional information about machine compliance correction because all of the experiments described in this chapter are performed without any crack opening gauge or strain gauge, such as a Linear Variable Differential Transformer (LVDT).

In order to evaluate machine compliance, the testing machine ram movement is recorded without any load (without the specimen installed) while attached LVDT is recording ram displacement at the same time. Based on an assumption that the testing machine ram movement without load is correct to within 1% error, the LVDT output and ram displacement are correlated as shown in Figure 5A-1. The LVDT has linear relationship with actual ram displacement: LVDT (V) = -0.01064 + 2.30393 × ram displacement (mm).

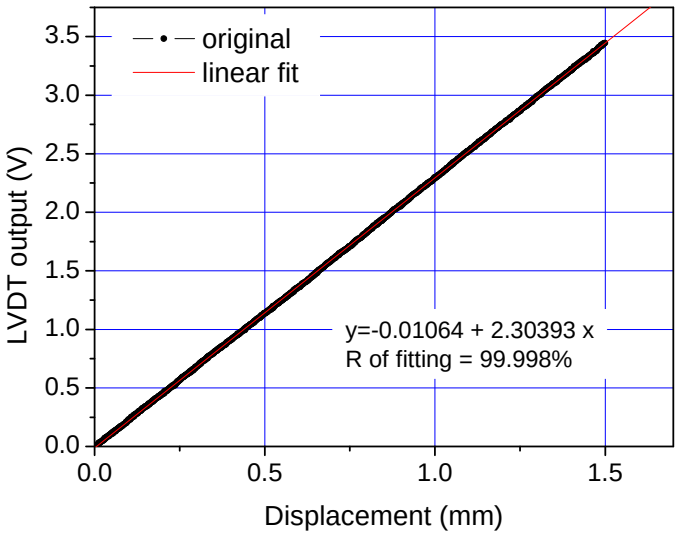

Figure 5A-1. Correlation between ram displacement and LVDT output voltage.

Then, loading is performed with the same set-up as the actual fracture test. As shown in Figure 5A-2, machine and fixture compliance exists. The difference between the ram movement reading and the LVDT reading is shown in Figure 5A-3: d_{mts}-d_{LVDT} = 0.0644 × load (kN). Applying the correction function to the actual load-displacement curve produces change shown in Figure 5A-4.

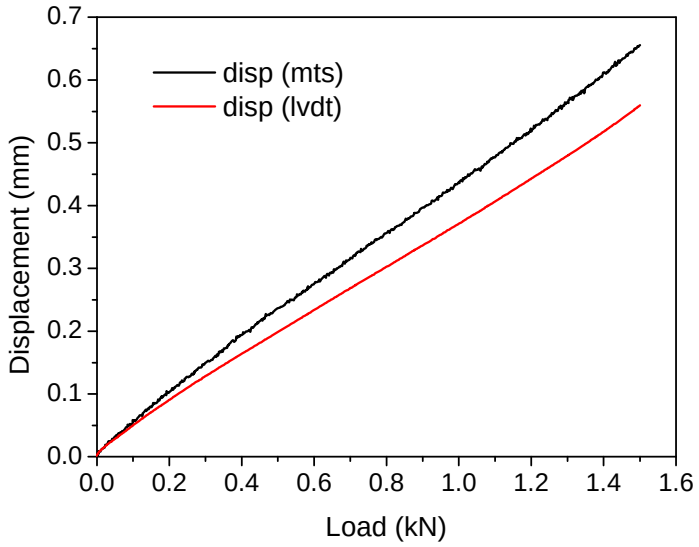

Figure 5A-2. Difference between ram displacement reading and LVDT displacement reading as a function of load applied.

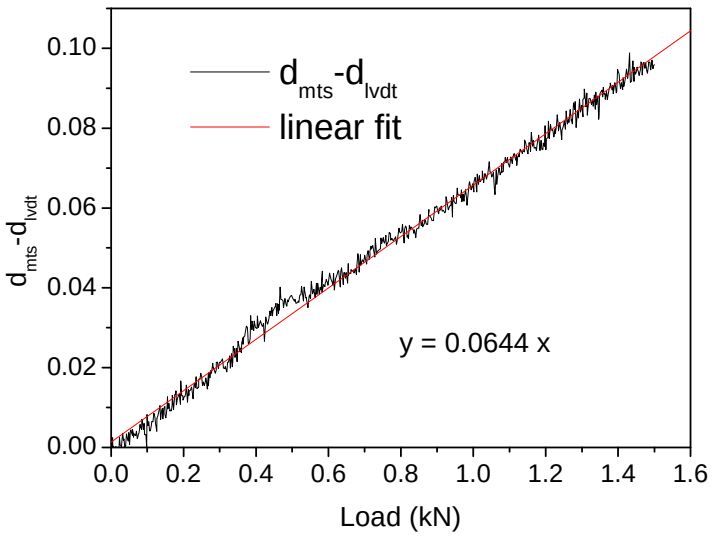

Figure 5A-3. A linear function to correct the machine and fixture compliance.

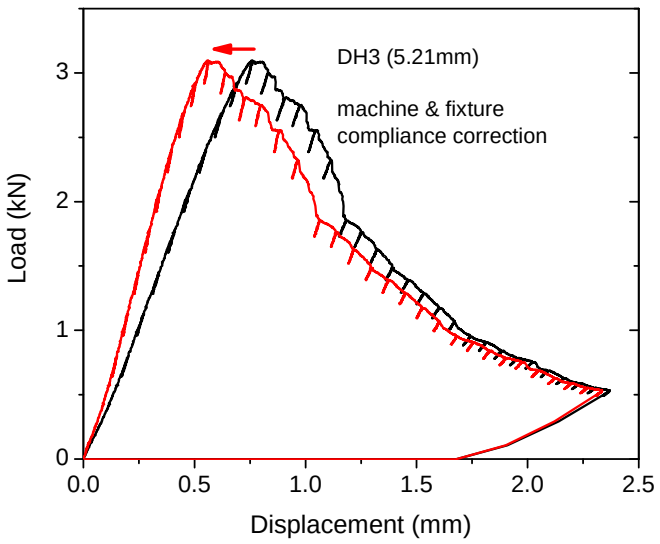

Figure 5A-4. Effect of machine and fixture compliance correction on load-displacement curve.